

The molecular emissions and the infall motion in the high-mass young stellar object G8.68-0.37

Zhiyuan Ren¹, Yuefang Wu¹, Ming Zhu², Tie Liu¹, Ruisheng Peng³, Shengli, Qin⁴, and Lixin Li^{1,5}

¹*Department of Astronomy, Peking University, 100871, Beijing China, E-mail: rzy,ywu@pku.edu.cn*

²*National Astronomical Observatory of China, 20A Datun Road, Chaoyang District, Beijing, China*

³*Caltech Submillimeter Observatory*

⁴*I. Physikalisches Institut, Universität zu Köln, Zùlpicher Str. 77, 50937*

⁵*The Kavli Institute for Astronomy and Astrophysics, Peking University, Yi He Yuan Lu 5, Hai Dian Qu, Beijing 100871, P.R. China*

30 August 2018

ABSTRACT

We present a multi-wavelength observational study towards the high-mass young stellar object G8.68-0.37. A single massive gas-and-dust core is observed in the (sub)millimeter continuum and molecular line emissions. We fitted the spectral energy distribution (SED) from the dust continuum emission. The best-fit SED suggests the presence of two components with temperature of $T_d = 20$ K and 120 K, respectively. The core has a total mass of up to $1.5 \times 10^3 M_\odot$ and bolometric luminosity of $2.3 \times 10^4 L_\odot$. Both the mass and luminosity are dominated by the cold component ($T_d = 20$ K). The molecular lines of $C^{18}O$, $C^{34}S$, DCN, and thermally excited CH_3OH are detected in this core. Prominent infall signatures are observed in the ^{12}CO (1–0) and (2–1). We estimated an infall velocity of 0.45 km s^{-1} and mass infall rate of $7 \times 10^{-4} M_\odot \text{ year}^{-1}$. From the molecular lines, we have found a high DCN abundance and relative abundance ratio to HCN. The overabundant DCN may originate from a significant deuteration in the previous cold pre-protostellar phase. And the DCN should now be rapidly sublimated from the grain mantles to maintain the overabundance in the gas phase.

Key words: stars: pre-main sequence — ISM: molecules — ISM: kinematics and dynamics — ISM: individual (G8.68-0.37) — stars: formation

1 INTRODUCTION

Gravitational infall, or core collapse can take place in high mass young stellar objects (YSOs) at early stages and continue all the way to the stage of Ultra Compact (UC) HII regions (Keto 2003; Sollins et al. 2005). As shown by theoretical works (Jijina & Adams 1996; Yorke & Sonnhalter 2002; Gong & Ostrike 2009, etc.), the infall motion is critical for initiating the high mass star formation and maintaining the accretion flow to feed the stellar mass during the subsequent evolutionary stages. However, further observations are still needed to better constrain the physical properties of the infall, including its spatial distribution, mass infall rate, chemical effect, and to understand its relation with other dynamical processes, including outflow, disk accretion, and core fragmentation. In the recent decade, extensive spectroscopic surveys (e.g. Wu & Evans 2003; Fuller et al. 2005; Wyrowski et al. 2006; Purcell et al. 2006; Wu et al. 2007) have been performed towards the potential high mass YSOs throughout the Milky Way. As a result, many infall candidates have been identified based on their spectral signatures. These sources can serve as good candidates to study the massive star birth and gas dynamics in the molecular cores. In the mean time, strong outflows are also widely detected towards those massive cores (e.g. Beuther et al. 2002; Wu et al. 2004; Zhang et al. 2007). The infall and outflow motions should be closely related and interacting with each other throughout the star formation history.

G8.68-0.37 (G8.68 here after) is a young high-mass star forming region at a distance of 4.5 kpc (Mueller et al. 2002). In this region, compact multiple gas-and-dust clumps has been discovered by Longmore et al. (2011, L11 here after). The dusty core is associated with strong 6.7 GHz methanol masers (Walsh et al. 1998), but has no radio continuum emission, indicating that high mass stars are already formed, but have not yet ionized its surrounding gas. L11 also detected a bi-polar outflow in CO (2 – 1). The outflow may be responsible for the shock interaction traced by the extended 4.5 μm emission (Figure 2 therein). In the mean time, the observation in HCO⁺ (1 – 0) suggests a plausible infall motion (Purcell et al. 2006) which should be examined quantitatively. To improve the understanding in physical and chemical properties of this source, we performed a multi-wavelength study using both the single dish antennae and the interferometers. The next section introduces the observations and data reduction, Section 3 presents the general observational results. Section 4 describes the dust continuum and molecular line emissions, wherein the infall signature is specifically described in Section 4.3. A summary is given in Section 5.

2 OBSERVATIONS AND DATA REDUCTION

2.1 The single dishes

In Figure 1 we show the central positions and the beam sizes of all the observations. We have observed G8.68 using three different single-dish telescopes. In 2005, we observed HCN (3-2) and H^{13}CO^+ (3-2) from the James Clerk Maxwell Telescope¹ (JCMT). The pointing center was adopted to be the coordinate of the strongest methanol maser (Walsh et al. 1998, with a position accuracy of $1.8''$), which is close to the continuum emission peak of L11 (cross in Figure 1). The mapping step is $10''$ (corresponding to 1/2 beam size), as shown in Figure 2b.

In November 2009, we observed $J = 1 - 0$ line of ^{12}CO , ^{13}CO , and C^{18}O using the 13.7 m telescope at the Purple Mountain Observatory² (PMO). The PMO observation contains a grid-mapping with a coverage of several arc minutes over the region of G8.68. In this paper, we only use the spectra at one point which is closest to the continuum peak, as shown in Figure 1. The PMO beam is much larger than the CSO and JCMT, and is significantly deviated from the continuum peak. Nevertheless, the beam has well covered the emission regions of the continuum and molecular lines. The data can thus be used to trace the gas motion on a larger scale near the core.

In May 2011, the $J = 2 - 1$ lines of the three CO isotopologues were observed from the 10 m telescope at the Caltech Submillimeter Observatory³ (CSO). The ^{12}CO (2-1) is observed at five symmetric points around the continuum peak with an offset of $\pm 23''$ in the R.A. and Dec. directions. Their positions are shown in Figure 2a. All the single-dish spectra are discussed in detailed in Section 3.2.2.

In Table 1, we present the basic observational parameters and weather conditions for the three instruments. In Table 2, we shows the more specific observational parameters for the molecular lines. All the observations were performed in good weather conditions, with pointing accuracies better than $5''$. GILDAS software package⁴ is used for the data reduction and image plot.

To measure the flux densities at different wavelengths, we also retrieved the Spitzer archival images at four IRAC bands from the GLIMPSE survey⁵, and the 24 and 70 μm images from

¹ JCMT is operated by the JAC, Hawaii, on behalf of the UK PPARC, the Netherlands OSR, and the Canadian NRC, see <http://www.jach.hawaii.edu/JCMT/>

² <http://www.dlh.pmo.cas.cn/>

³ <http://www.submm.caltech.edu/cso/>

⁴ <http://iram.fr/IRAMFR/GILDAS/>

⁵ Available at <http://irsa.ipac.caltech.edu/>, see also Benjamin et al. (2003).

MIPSGAL⁶, and JCMT/SCUBA images at 450 and 850 μm bands, which are available at the Canadian Astronomy Data Center (CADC) repository of the SCUBA Legacy Fundamental Object Catalogue⁷.

2.2 The Submillimeter Array

The Submillimeter Array⁸ (SMA) observations towards G8.68 are taken from the released SMA data archive. The observations are made in three epochs in the year 2007, 2008, and 2009, respectively. The observational parameters, including the calibration sources for each epoch are presented in Table 3. In all three epochs, the compact array was used, and the phase tracking center is R.A.(J2000)=18^h06^m23.23^s, Dec.(J2000)=-21°37'14.19". The three observations have similar beam sizes for the synthesized and primary beams. In Figure 1, we only show the beams of the 2008 observation in order to have a clear appearance. The observed gas-and-dust structures (Figure 4) turn out to be smaller than the SMA primary beam. Thus the beam-edge weakening is not significant. The calibration and imaging were performed in Miriad¹. The absolute flux level has an uncertainty of $\sim 15\%$. The continuum emission was subtracted from the line-free channels in each sideband. The gain solution is self-calibrated for the continuum image and then exported to the spectral line data.

We note that among the SMA data, the 2008 observation has the longest on-source integration time hence the lowest noise level. In addition, in 2008 all eight antennae of the SMA were at work, while the 2007 observation (280 GHz) only employed seven antennae. As a result, despite its higher frequency, the 2007 data has a lower angular resolution than the 2008 data (as indicated by their synthesized beam sizes, in Table 3). We therefore used the 2008 data (frequency centered at 225 GHz, or 1.3 mm) to analyze the dust continuum emission. The continuum was averaged from the line-free channels and then subtracted from the side-band spectrum. The continuum data of the two sidebands were averaged on the (u,v) plane and then converted to the image domain. After Clean and Self-calibration, the 1.3 mm continuum image has an rms noise level (1σ) of 3.6 mJy beam⁻¹ (corresponding to a brightness temperature of $T_b = 0.0025$ K).

⁶ <http://irsa.ipac.caltech.edu/>

⁷ <http://www4.cadc-ccda.hia-ihp.nrc-cnrc.gc.ca>

⁸ The Submillimeter Array is a joint project between the Smithsonian Astrophysical Observatory and the Academia Sinica Institute of Astronomy and Astrophysics and is funded by the Smithsonian Institution and the Academia Sinica, see <http://www.cfa.harvard.edu/sma/>

3 RESULTS

3.1 Dust continuum emission

In Figure 4, we show the continuum emissions of G8.68 from infrared to (sub)millimeter wavebands, including the IRAC 3.6, 4.5, and 8 μm emissions (RGB color image), the SMA 1.3 mm continuum emission (white contours), and the SCUBA 450 μm continuum (blue dashed contours).

Figure 4 is centered at the 1.3 mm continuum peak, the coordinates of which are R.A.(J2000)= $18^{\text{h}}06^{\text{m}}23.52^{\text{s}}$, Decl.(2000)= $-21^{\circ}37'11''$. It is close in projection to the SMA phase tracking center (labeled with the red cross). After deconvolution with the synthesized beam, the core has an angular size of $11'' \times 6''$ for the 4σ contour (0.24×0.13 pc at a distance of 4.5 kpc). It is elongated in the north-south direction ($PA = -10^{\circ}$ for the major axis), reasonably coherent with the 4.5 μm emission (green color). Since the 4.5 μm emission traces the shock interaction between the outflow and the envelope gas, it is possible that the outflow and shocks are also affecting the dust distribution, causing its observed elongation. We did not find any evidence for multiple sub-cores either in our 1.3 mm continuum or any molecular lines (Figure 5). Therefore the gas-and-dust core should have a single compact morphology, and the fragmentation is not evident on our observational scale (0.05 to 0.5 pc).

More diffused dust component can be revealed by the SCUBA 450 μm continuum emission. As shown in Figure 4, the 450 μm emission is more extended and less elongated than the 1.3 mm emission. We use the average deconvolved FWHM (full width at half maximum) radius $\langle r \rangle$ to represent the extent of the continuum and molecular line emissions. Normally $\langle r \rangle$ can be measured from the 50 % contour level of the emission region. However, the 50 % contour (for the continuum and molecular lines) is often close to or even smaller than beam size. We thus suggest measuring the deconvolved radius from the 10 % contour, and adopt its 1/2 as the value of $\langle r \rangle$. For the continuum images, the 10 % contour is not specifically plotted in Figure 4, but close to the 14σ and 4σ contour level for the 1.3 mm and 450 μm emissions, respectively. We obtained $\langle r \rangle_{450\mu\text{m}} = 0.23$ pc and $\langle r \rangle_{1.3\text{mm}} = 0.08$ pc.

We also measured the integrated flux density $F(\lambda)$ of the dust core at wavelength λ . In general, we use the 4σ emission level as the integration area for $F(\lambda)$. As an exception, for the IRAC data, we use the region of the 4.5 μm emission (green color in Figure 4) to measure the integrated flux of all four bands, since the 4.5 μm emission has a relatively clear boundary. The 5.8 μm band shows a similar morphology with the 4.5 μm , while the emissions at other two bands

are much fainter and cannot be well delineated. The IRAC stellar sources in the vicinity of the core are carefully excluded from the integration area. The derived $F(\lambda)$ are shown in Table 4.

3.2 Molecular lines

3.2.1 The Submillimeter Array

Using the SMA, we have detected a number of molecular transitions of $C^{18}O$, $C^{34}S$, DCN, and CH_3OH . Their beam-averaged spectra towards the 1.3 mm continuum peak and their velocity-integrated intensity images are shown in Figure 5. For the CH_3OH , altogether we have detected 11 rotational transitions. We selected five of them with largely different E_u , and presented their images in Figure 5. The physical parameters of all the molecular transitions are shown in Table 5.

As shown in Figure 5, the spectra of the molecular tracers of high-density gas mostly show lines with single peak profiles. As exceptions, there are two CH_3OH lines, $11_2 - 10_3$ ($E_u = 191$ K) and $15_{7,8} - 16_{6,11}$ ($E_u = 523$ K) which show double peak profiles. However, since the remaining lines are all single-peaked, the two lines are more likely to be blended with other molecular transitions. The possible candidates for the blenders are NH_2CN $14_2 - 13_2$ ($f=279.35062$ GHz, $E_u = 228$ K) and $HCCNC$ $29 - 28$ ($f=288.07346$ GHz, $E_u = 207$ K). We used two gaussian profiles to fit the blended spectra, as plotted in dotted lines in Figure 5. For each spectrum, the peak velocity of the second component is well consistent with the anticipated velocity for the blenders. With the contamination excluded, these two CH_3OH lines should also have single gaussian profiles.

The $C^{34}S$ emission region shows an elongated morphology from the northeast to southwest ($PA = 45^\circ$) as labeled in dashed line. The elongation agrees with the orientation of the CO outflow and $4.5 \mu m$ shock emission (Figure 4). An elongated morphology towards northeast is also shown in the low excited CH_3OH lines (i.e. $E_u = 33$ K and 97 K). Therefore, both the CH_3OH and $C^{34}S$ distributions should be affected by the outflow. The $C^{18}O$ ($2 - 1$) also shows a non-regular morphology. However, it is biased to the south of the dust core, peaked at offset= ($0''$, $-2''$). In addition, the $C^{18}O$ shows a secondary clump in the southeast, peaked at offset= ($10''$, $-8''$). This clump is not detected in $C^{34}S$ or CH_3OH lines, indicating that it may be depleted in these species. The $C^{18}O$ might trace cooler and less dense gas component, thus have a more extended feature than other dense-core species. For each molecular transition, we also measured the av-

erage deconvolved radius from the 10 % contour level (and adopted its 1/2 as the value of $\langle r \rangle$). The results are shown in Table 5.

3.2.2 The single dishes

Figure 2 and 3 show the molecular lines detected from the single dishes. As shown in Figure 3, prominent double-peak line profiles are observed in the ^{12}CO (1 – 0), (2 – 1), and also HCN (3 – 2). For both the ^{12}CO (1 – 0) and (2 – 1), the blueshifted emission peak is much stronger than the redshifted one, and the central absorption dip is well coincident with the C^{18}O line peak ($V_{\text{lsr}} = 37 \text{ km s}^{-1}$). Such blue asymmetric ^{12}CO lines suggest the presence of infall motion towards the core center (Zhou et al. 1993; Mardones et al. 1997). For the physical explanation, when the infall occurs in the envelope which is cooler than the inner region, the gas in the front part would absorb the redshifted side of the line profile, whereas the gas in the rear part (behind the center) would increase the blueshifted emission because it is moving towards the observer. Besides the infall signature, the ^{12}CO lines also exhibit high-velocity emission wings extending to $V_{\text{lsr}} = 25$ and 50 km s^{-1} for the blue- and redshifted sides, respectively. This velocity range is comparable to the outflow velocities revealed by L11 (Figure 5 therein).

The two ^{13}CO lines also have a blueshifted emission peak ($V_{\text{lsr}} = 35 \text{ km s}^{-1}$) with respect to the C^{18}O , suggesting that the ^{13}CO is also probably tracing the infall motion. However, because the ^{13}CO lines are much less optically thick than the ^{12}CO , they exhibit no central dip, but instead show an emission shoulder that continuously declines towards the redshifted side.

As shown in Figure 2a, we can see that the offset positions also exhibit self-absorbed profiles (except the southeast one). However, compared to the central spectrum, their blue- and redshifted peaks have more similar intensities. As an extreme, the southeastern spectrum have a flattened top, with the double-peak feature almost disappeared. This indicates that the infall motion (along the line of sight) should have a decline towards those offset points. And their distance from the center (0.7 pc) can therefore be taken as a lower limit for the radius of the infalling region.

As shown in Figure 3c, the HCN (3 – 2) has a double peak profile and high-velocity emission wings extending to $V_{\text{lsr}} = 29$ and 53 km s^{-1} (above the noise level) for the blue and red wings, respectively. However, its double peaks have different asymmetry with the ^{12}CO lines, i.e., the red peak is slightly stronger than the blue one. The offset spectra of the HCN (Figure 2b) have much lower signal-to-noise ratio (mainly due to their shorter integration time). How-

ever, they still evidently show double peak profiles, and have similar intensities for the blue and red peaks. Like in the case of the CO lines, the optically thin isotopic lines, i.e., DCN (3–2) and (4–3) are both single-peaked, hence the HCN (3–2) profile should originate from a self absorption effect. Compared to the ^{12}CO profiles, the HCN spectra may reflect different gas motions, including core expansion or/and rotation (Pavlyuchenkov et al. 2008). In particular, as the most possible case, a cold and spherically expanding envelope would cause a prominent blueshifted self-absorption towards the center, while at the offset positions, the expansion should be on the plane of the sky, thus show a less blueshift due to the lower radial velocities. This scenario can reasonably explain the observed line profiles, but still needs a further examination with an improved angular resolution and spectral sensitivity. In Figure 2b, we also plotted the velocity-integrated map of HCN (3–2) (discrete gray scales). We measured the average deconvolved radius $\langle r \rangle$ of HCN from its 50 % contour. As a result, it has $\langle r \rangle = 12''$ (and $\eta_{\text{bf}} = 1$).

Another JCMT line, H^{13}CO^+ (3–2), has a regular gaussian profile, indicating that it may arise from the dense molecular core and is not evidently affected by the infall or outflow motion. We only have one-point observation for the H^{13}CO^+ (3–2) at the continuum center, and in calculation for its column density (Section 4.4), we assume $\eta_{\text{bf}} = 1$.

4 DISCUSSION

4.1 The physical properties of the dust core

As shown in Figure 4, the 1.3 mm dust core does not coincide with any infrared stellar sources besides the extended $4.5\ \mu\text{m}$ shock emission. This indicates that the stellar emission from the core center is highly obscured by the dust. In the vicinity of the 1.3 mm dust core, a few stellar objects are shown in the IRAC RGB image (also labeled with the asterisks). All these objects are isolated from the 1.3 mm continuum emission, yet the three objects nearest to the continuum peak are likely to be embedded in the $450\ \mu\text{m}$ emission region. They might either be more evolved young stars in the same star forming region or irrelevant foreground stars. Despite this uncertainty, it is clear that these objects have no significant contribution to the dust continuum or molecular line emissions. We therefore make no further discussion for them.

We can fit the Spectral Energy Distribution (SED) of the dust core from its flux densities at the Spitzer and JCMT/SCUBA wavebands. Assuming a gray body emission and a uniform dust temperature T_{d} , the continuum flux density would be (Schnee et al. 2007)

$$F_\nu = \frac{M_{\text{core}} \kappa_\nu B_\nu(T_d)}{g D^2} \quad (1)$$

where F_ν is the flux density at frequency ν . M_{core} is the total gas-and-dust mass of the core. $g = 100$ is commonly adopted gas-and-dust mass ratio. $B_\nu(T_d)$ is the Planck function at temperature T_d . $D = 4.5$ kpc is the source distance. The dust opacity κ_ν is assumed to have a power-law shape, i.e. $\kappa_\nu = \kappa_{230\text{GHz}}(\nu/230\text{GHz})^\beta$, with the reference value $\kappa_{230\text{GHz}} = 0.9 \text{ cm}^2 \text{ g}^{-1}$ (Ossenkopf & Henning 1994). The free parameters in the fit are M_{core} , T_d , and β . We found that the emissions from $8 \mu\text{m}$ to $850 \mu\text{m}$ can be best fitted with two temperature components which have $T_d = 20 \text{ K}$ and 120 K respectively, and $\beta = 2.1$. The best-fit SED is shown in Figure 6.

We did not include the IRAC 3.6, 4.5 or $5.8 \mu\text{m}$ emissions in our SED model. The 4.5 and $5.8 \mu\text{m}$ emissions may largely come from the shocked emission thus are much stronger than the emissions at other two IRAC bands (Table 4). As for the $3.6 \mu\text{m}$ emission, if being thermally excited, it may arise from some even hotter component which is much fainter and poorly constrained by our current data. Therefore we also neglected the $3.6 \mu\text{m}$ band. With the derived SED, the bolometric luminosity can be estimated using $L_{\text{bol}} = 4\pi D^2 \int F_\nu d\nu$. As a result we have $L_{\text{bol}} = 2.3 \times 10^4$ and $8 \times 10^2 L_\odot$ for the cold (20 K) and warm (120 K) components, respectively. Using Equation (1), we can also estimate the total mass of the two temperature components, which turn out to be 1.3×10^3 and $1.0 \times 10^{-3} M_\odot$ for the 20 K and 120 K components, respectively. One can see that both the core mass and luminosity are dominated by the gas-and-dust component which is characterized by $T_d = 20 \text{ K}$.

In Equation (1), by replacing the integrated flux density F_ν with the flux density at the continuum peak ($0.32 \text{ Jy beam}^{-1}$), and then dividing the obtained mass with the beam area and the average molecular mass (1.4 times the molecular mass of H_2), we can derive the H_2 column density $N(\text{H}_2)$ towards the continuum peak. And then, assuming that the core is approximately spherical, we can derive the volume number density using $n(\text{H}_2) = N(\text{H}_2)/2\langle r \rangle$. The physical parameters of the dust core are presented in Table 4.

By extrapolating the best-fit SED curve, we can get a flux density of 2.9 Jy at $\lambda = 1.3 \text{ mm}$. Compared to this value, the SMA observation has recovered 35% of the 1.3 mm continuum emission. Adopting $T_d = 20 \text{ K}$, we also estimated the physical parameters from the SMA 1.3 mm continuum, which are presented in Table 4. Based on the continuum observations, we suggest that the gas-and-dust core in G8.68 should consist of a dense inner region (characterized by the 1.3 mm emission), and a more extended envelope (traced by the $450 \mu\text{m}$ emission).

4.2 The CH₃OH rotational temperature

The molecular gas temperature can also be estimated from the CH₃OH lines using the rotation diagram. The methanol lines all have linewidths of several km s⁻¹, with none of them showing abnormally high intensities, therefore the CH₃OH lines are unlikely to have maser excitations.

Assuming optically thin, the column density of the upper-level N_u can be derived from the integrated line intensity using (Tielens 2005)

$$N_u = \frac{8\pi k v_{ul}^2}{hc^3 A_{ul}} \int T_b dV / \eta_{bf} \quad (2)$$

where T_b is the observed brightness temperature. A_{ul} is the Einstein coefficient in s⁻¹. η_{bf} is the beam filling factor. All other constants take their usual values in SI units. Although for an emission line, η_{bf} may vary at different velocities, we approximate it to be a single value as the ratio between the integrated emission region and the beam area, i.e., $\eta_{bf} \simeq \pi \langle r \rangle^2 / A_{beam}$ (used when the emission region is smaller than the beam size, otherwise $\eta_{bf} = 1$). η_{bf} is estimated for each transition and the derived values are presented in Table 5 (Column 11).

Assuming a Local Thermal Equilibrium (LTE, i.e. energy levels are populated according to a Boltzmann distribution characterized by a single temperature), the relation between the total column density N_T and N_u is

$$\frac{N_u}{g_u} = \frac{N_T}{Q(T_{rot})} \exp\left(-\frac{E_u}{kT_{rot}}\right) \quad (3)$$

and its logarithmic form is

$$\ln\left(\frac{N_u}{g_u}\right) = \ln\left(\frac{N_T}{Q(T_{rot})}\right) - \frac{E_u}{kT_{rot}} \quad (4)$$

where g_u and E_u are the degeneracy and the excitation energy of the upper level, respectively, and $Q(T_{rot})$ is the partition function. For CH₃OH, a good approximation is $Q(T_{rot}) \simeq 1.2327 \times T_{rot}^{1.5}$ (Townes & Schawlow 1955).

The rotation diagram for the CH₃OH lines is shown in Figure 7. A linear least-square fit to the data points results in $T_{rot} = 130 \pm 10$ K and $N_T = (5.3 \pm 0.6) \times 10^{15}$ cm⁻².

In the calculation, in order to correct for the optical depth effect, one should multiply N_u/g_u with a correction factor $C_\tau = \tau / (1 - e^{-\tau})$ and fit the rotational temperature iteratively. The optical depth is estimated using (Remijan et al. 2004, Equation (3) therein, slightly reformed)

$$\tau = \frac{c^3 \sqrt{4 \ln 2}}{8\pi v^3 \sqrt{\pi} \Delta V} N_u A_{ul} \left[\exp\left(\frac{hv}{kT_{rot}}\right) - 1 \right] \quad (5)$$

Among all the CH₃OH lines, the (8₋₁ – 7₀) transition has the highest optical depth ($\tau = 0.059$). The other lines are even more optically thin. To take into account the temperature uncertainty,

we also estimated the optical depth assuming $T_{\text{rot}} = 20$ K which is a lower limit as suggested by the SED fitting. At 20 K, the optical depths become ~ 8 times larger than the values at $T_{\text{rot}} = 130$ K. The derived optical depths are listed in Table 5, and the column densities and abundances are listed in Table 6.

The rotational temperature of $T_{\text{rot}} = 130$ K is close to the SED temperature of the warm dust component ($T_{\text{d}} = 120$ K). Therefore it is possible that the CH_3OH emissions are mainly from the region associated with the warm dust. Moreover, since the cold component ($T_{\text{d}} = 20$ K) is more massive than the warm one for orders of magnitude, the CH_3OH may have a severe depletion in the region for the cold dust component. However, it is also possible that the dust and gas are thermally decoupled, thus exhibit different temperatures. The collisional excitations of the molecular gas can be particularly enhanced by the shocks (especially along the outflow direction), thereby showing a high value of T_{rot} . The dust temperature T_{d} , in comparison, may still be largely dominated by the stellar heating thus has a much lower value.

4.3 The CO emission and the infall motion

As shown in Section 3.2.2, both the infall and outflow signatures are detected in the ^{12}CO (2–1) and (1–0) lines. In this paper we mainly discuss the infall properties based on the ^{12}CO (2–1). We first make attempt to separate the different components from the observed spectrum, then estimate the infall rate.

Following the procedure of Purcell et al. (2006), we used a broad gaussian profile to fit the outflow wings (velocity range of $V < 32$ and $V > 42$ km s $^{-1}$), and then subtracted it from the spectrum. The residual line profile (green line in Figure 8) should mainly represent the emission from the dense molecular core. One can then mask the velocity range possibly affected by the infall motion (34 to 43 km s $^{-1}$), and make a gaussian fit to the spectrum outside this velocity range. The fitted spectrum is speculated to roughly represent the molecular core emission unaffected by the infall signature. However, for the ^{12}CO lines, due to its large optical depth, we cannot directly apply a Gaussian fit to the spectrum. Instead, one should model the spectrum using the radiation transfer function. In this case, the line profile can be expressed as

$$T_{\text{mb}}(V) = [T_{\text{mb},0} - J(T_{\text{CMB}})][1 - e^{-\tau(V)}] \quad (6)$$

$J(T) = T_0 / [\exp(T_0/T) - 1]$ is the Planck-corrected brightness temperature, and $T_0 = h\nu/k$. $T_{\text{CMB}} = 2.7$ K is the temperature of the cosmic background. At the frequency of CO (2–1) (230 GHz), we

have $J(T_{\text{CMB}}) = 0.2$ K. Compared to the intensity of the CO emission, the contribution from the cosmic background can be almost neglected.

We also assume the dense molecular core to have a uniform gas distribution along the line of sight, with central velocity V_0 , velocity dispersion σ and peak optical depth τ_0 . Then the optical depth is

$$\tau(V) = \tau_0 \exp\left[-\frac{(V - V_0)^2}{2\sigma^2}\right] \quad (7)$$

where σ is related to the (intrinsic) line width ΔV by $\sigma = \Delta V / \sqrt{8 \ln 2}$. In an optically thick case, the line emission could be largely saturated. τ_0 is thus poorly constrained by the observed spectrum. However, it can be estimated from comparison to the CO isotopologues following Garden et al. (1991, Equation (4) therein). Since the ^{13}CO is also affected by the infall motion, we used the C^{18}O (2 – 1) instead. Assuming an abundance ratio of $[^{12}\text{CO}/\text{C}^{18}\text{O}] = 490$ (Garden et al. 1991), the equation will be

$$\frac{T_{\text{mb},0}(^{12}\text{CO})}{T_{\text{mb},0}(\text{C}^{18}\text{O})} = \frac{1 - \exp[-\tau_0(^{12}\text{CO})]}{1 - \exp[-\tau_0(\text{C}^{18}\text{O})]} = \frac{1 - \exp[-\tau_0(^{12}\text{CO})]}{1 - \exp[-\tau_0(^{12}\text{CO})/490]} \quad (8)$$

To fit the line profile, we first take an arbitrary, but reasonable value of τ_0 , and then fit the line profile by adjusting the values of $T_{\text{mb},0}$, V_0 and ΔV in Equation (6) and (7). The best-fit $T_{\text{mb},0}$ is then used to estimate τ_0 again using Equation (8). The final best fit can be reached after two or three iterations. Eventually, we have $T_{\text{mb},0} = 32$ K, $\Delta V = 5.5$ km s $^{-1}$, $V_0 = 37$ km s $^{-1}$, and $\tau_0(^{12}\text{CO}) = 68$. In Figure 8, the best fit spectrum is shown in dashed line. And a sum of dense-core and outflow components is shown in red dot-dashed line. The output spectrum has an apparent line width of 8.5 km s $^{-1}$ which is indeed much broader than the intrinsic ΔV . We fit the ^{12}CO (1 – 0) using the same method. All their line parameters are listed in Table 5 (Column 5 to 8).

The infall rate is estimated using (Klaassen & Wilson 2007)

$$\dot{M}_{\text{infall}} = \frac{4}{3} \pi n(\text{H}_2) \mu m_{\text{H}} r_{\text{gm}}^2 V_{\text{in}} \quad (9)$$

wherein r_{gm} is geometric mean radius of the core, $n(\text{H}_2)$ is the ambient source density, and V_{in} is the typical infall velocity. In calculation we estimated V_{in} from the outflow-subtracted line profile using Equation (9) in Myers et al. (1996). As a result we have $V_{\text{in}} = 0.45$ km s $^{-1}$. In addition, we assume that the more diffused gas traced by the 450 μm emission which has $n(\text{H}_2) = 0.8 \times 10^6$ cm $^{-3}$, is collapsing towards the dense inner region characterized by the 1.3 mm continuum (Figure 4), thus we have $r_{\text{gm}} = \langle r \rangle_{1.3\text{mm}} = 0.08$ pc. With these assumptions, we derived an infall rate of $\dot{M}_{\text{infall}} = 7.0 \times 10^{-4} M_{\odot} \text{yr}^{-1}$.

As seen in Equation (9), the derived infall rate is sensitive to the adoption of r_{gm} , and our currently adopted r_{gm} is relatively conservative. Adopting $r_{\text{gm}} = \langle r \rangle_{450\mu\text{m}} = 0.23$ pc, we would have $\dot{M}_{\text{inf}} = 5 \times 10^{-3} M_{\odot} \text{ yr}^{-1}$. However, we note that such a large-scale estimate may deviate from the small-scale infall rate. To resemble the mass infall onto the central stars, it may be more reasonable to adopt the first value ($r_{\text{gm}} = 0.08$ pc). With the obtained infall rate, we then estimate the accretion luminosity, using $L_{\text{acc}} = GM_* \dot{M}_{\text{inf}} / R_*$, and assuming a mass-radius relation of $R_* / R_{\odot} = (M_* / M_{\odot})^{0.8}$. As a result, we have $L_{\text{acc}} = (4 \pm 2) \times 10^4 L_{\odot}$. The uncertainty in L_{acc} corresponds to a stellar mass varying between 10 and 100 M_{\odot} . It is likely that the bolometric luminosity of the dust core ($2.3 \times 10^4 L_{\odot}$, see Section 4.1) should have a major energy supply from the accretion process.

Considering the existence of the outflow, there should be a strong interaction between the infall and the outflow. And the interaction may be responsible for the 4.5 μm shock emission. Chen et al. (2010) have performed an HCO^+ (1-0) survey towards the Extended Green Objects (EGOs), i.e., the massive YSO candidates with the 4.5 μm shock emissions. They found that nearly one third of the sample (29 out of 69 sources) exhibit a significant blue asymmetry. While in an HCO^+ (1-0) survey towards 82 massive YSOs selected from the methanol masers, only 12 sources have infall signatures (Purcell et al. 2006). Comparing these results, it is likely that the shocks are prone to take place in the YSOs with infall motions. This is theoretically expected, since compared to an interaction between the outflow and quiescent gas, an outflow-infall interaction would more efficiently convert the kinetic energy into heat and radiation.

4.4 The molecular abundances and DCN overabundance

The total column density $N_{\text{T}}(\text{X})$ and abundance $f(\text{X}) = N_{\text{T}}(\text{X}) / N(\text{H}_2)$ of the C^{18}O , HCN, DCN, H^{13}CO^+ , and C^{34}S are calculated from their emission lines at the continuum emission peak using equation (2) and (3). And a correction for the optical depth is done using Equation (4). To derive the HCN and H^{13}CO^+ abundances, we used the $N(\text{H}_2)$ value for the SCUBA 450 μm continuum (Table 3). While for the SMA lines, we adopted $N(\text{H}_2)$ from the 1.3 mm continuum ($0.95 \times 10^{24} \text{ cm}^{-2}$). We also note that $N_{\text{T}}(\text{H}^{13}\text{CO}^+)$ may be underestimated due to the beam dilution thus should be regarded as a lower limit. To take into account the temperature uncertainty, we also estimated $N_{\text{T}}(\text{X})$ at the lower limit of $T_{\text{rot}} = 20$ K (suggested by the SED fitting). The $N_{\text{T}}(\text{X})$ and $f(\text{X})$ values are shown in Table 6.

In calculation of the HCN, its line profile should be corrected for the self absorption. We

modeled its original line profile using the same method for the ^{12}CO (2 – 1) (Section 4.2). However, since the abundance ratio between DCN and HCN is much more uncertain than $[\text{C}^{18}\text{O}/^{12}\text{CO}]$, we cannot use DCN to reliably determine the optical depth of HCN (3 – 2). Nevertheless, we expect the HCN (3 – 2) to have a low optical depth due to two reasons. Firstly, since the HCN (3 – 2) likely traces denser and hotter gas than the ^{12}CO (2 – 1), if the HCN (3 – 2) has a very large optical depth, it should have a comparable intensity with the ^{12}CO (2 – 1). Nevertheless, even after the self-absorption correction, the HCN (3 – 2) is still much weaker than the ^{12}CO (2 – 1). Second, with an apparent line width ($\Delta V = 6.2 \text{ km s}^{-2}$) being close to ΔV of the C^{18}O and CH_3OH lines (as shown in Table 5), the optical-depth broadening should be insignificant for the HCN (3 – 2). We therefore directly calculate $N_{\text{T}}(\text{HCN})$, and then estimate the optical depth using Equation (5). As a result, we found $\tau = 0.78$ at $T_{\text{rot}} = 20 \text{ K}$ and 0.10 at 130 K. This result is consistent with our expectation. However, to more accurately determine the HCN optical depth, one should consider to observe some other isotopologues such as HC^{15}N (Hatchell et al. 1998).

From the derived abundances, we can get a relative abundance ratio between DCN and HCN which is $[\text{DCN}/\text{HCN}] \approx 0.07$. The values derived at the two temperature limits are similar to each other (Table 6). Compared to the cosmic $[\text{D}/\text{H}]$ ratio (10^{-5} , Linsky 1998), the $[\text{DCN}/\text{HCN}]$ in G8.68 implies a deuteration for orders of magnitudes. The $[\text{DCN}/\text{HCN}]$ in G8.68 is also much higher than the values detected in hot molecular cores (10^{-4} to 10^{-3} , Hatchell et al. 1998). However, it is much more comparable to the abundance ratio of $[\text{N}_2\text{D}^+/\text{N}_2\text{H}^+]$ detected in high-mass YSOs in the infrared dark clouds (Chen et al. 2011). Overabundant DCN was previously detected in a number low-mass YSOs (Roberts et al. 2002), while in high-mass star-forming regions, the DCN is not frequently detected.

The overabundant DCN in G8.68 may originate from a high level of deuterium fractionation in the previous cold pre-stellar phase. In highly deuterated gas (abundant in H_2D^+ , CH_2D^+ , C_2HD^+ etc.), DCN can be produced via D-H substitution of the HCN, or through more complex reaction pathways (Albertsson et al. 2011, Reaction (17) to (21) therein). Finally the DCN molecules would mostly reside on the grain mantles (Hatchell et al. 1998; Roberts et al. 2002). During the star formation, the DCN can be released into the gas-phase again. However, once the temperature slightly increases, the gas-phase DCN can be easily destroyed via reactions such as

$\text{H} + \text{DCN} \rightarrow \text{HCN} + \text{D}$ (Charnley et al. 1992; Roberts et al. 2002, Figure 5 therein). In this sense, to maintain the DCN overabundance in the gas, two conditions may have to be satisfied. First, there should be a high-level deuterium fractionation in the previous dark-cloud phase. Second,

in order to compensate the chemical destruction due to the stellar heating, a rapid sublimation for the dust grains should be necessary. Again, the outflow and shocks may have a potential contribution to this process. However, unlike the $C^{34}S$ and CH_3OH , the DCN emission has a compact and spherical morphology which is not evidently coherent with the outflow. Therefore it is possible that the DCN enhancement is less affected by the shocks and/or more sensitive to the stellar heating. A higher sensitivity and spatial resolution may help better reveal the DCN morphology and determine whether it is associated with the outflow.

As another possibility, the DCN can also be synthesized in the recent gas phase chemistry. Parise et al. (2009) show that the gas-phase reactions may sufficiently account for the enhanced D-H ratio in the molecular gas in the Orion Bar PDR, which has a [DCN/HCN] ratio of 10^{-2} , comparable with that in G8.68. However, the gas-phase enhancement may have to proceed in an environment with stable lukewarm heating. This condition may hardly be satisfied in regions with rapid evolution of the high-mass stars. Therefore the grain mantle sublimation may still be the major process for the DCN enhancement in G8.68. In the future study, one can compare other chemical products from the grain sublimation and gas-phase chemistry in order to determine the relative importance of these two processes.

The $C^{34}S$ abundance in G8.68 is much lower than the average $C^{34}S$ abundance in the UC HII regions (Olmi & Cesaroni 1999). $f(C^{18}O)$ is also much smaller than the typical ISM value (1.7×10^{-7} , Frerking et al. 1982). Compared to the ISM abundance, it has a depletion factor of $f_D(C^{18}O) = 5 \pm 2$.

5 SUMMARY

We have investigated the dust continuum and molecular line emissions towards the high mass YSO G8.68-0.37. We have revealed a dense compact gas-and-dust core in the SMA 1.3 mm continuum emission, and its more extended envelope in the SCUBA 450 μm emission. At our angular resolution (spatial scale > 0.05 pc), there is no evident fragmentation structures. We find that an SED with at least two temperature components is necessary to account for the dust continuum emissions from mid-IR to submillimeter wavelengths. The best-fit temperatures for the two components are $T_d = 20$ K and 120 K. The core mass and luminosity are mainly contributed by the cold component ($T_d = 20$ K).

Prominent infall signatures and outflow wings are detected in both ^{12}CO (1 – 0) and (2 – 1) lines. We separated the outflow and dense-core components and measured their line param-

eters. The ^{12}CO (2 – 1) yields an infall velocity of 0.45 km s^{-1} . Assuming that the extended envelope is collapsing towards the inner dense region, we can derive an infall rate of $7 \times 10^{-4} M_{\odot} \text{ year}^{-1}$. It is possible that the $4.5 \mu\text{m}$ shock emission is largely enhanced by a strong interaction between the infall and outflow motions. In addition, we also suggest that the infall motion may be important for suppressing the stellar emissions thereby protecting the DCN and other fragile species.

We estimated a rotational temperature of 130 K from the CH_3OH lines. We derived the abundances of the molecular species from their spectra, and in particular, we found a high abundance ratio of $[\text{DCN}/\text{HCN}] = 0.07$. The over abundant DCN may originate from a high-level of deuterium fractionation in the previous pre-protostellar phase, as well as the recent grain mantle sublimation and/or gas-phase chemistry. More details in this chemical process are still to be further investigated.

ACKNOWLEDGMENT

We are grateful to the SMA observers and the SMA data archive. We would thank the anonymous reviewer for the detailed, thoughtful comments and suggestions helping us to largely improve the presentation and interpretation. This work is supported by the NSFC grants of No.10733033, 10873019, 10973003, and the NKBRP grants of 2009CB24901 and 2012CB821800.

REFERENCES

- Albertsson, T., Semenov, D., Henning Th., 2011, astro-ph: 1110.2644
- Benjamin, R. A., et al. 2003, PASP, 115, 953
- Bergin, E. A., Alves, J., Huard, T., & Lada, C. J. 2002, ApJ, 570, L101
- Beuther, H., Schilke, P., Menten, K. M., Motte, F., Sridharan, T. K., Wyrowski, F. 2002, ApJ, 566, 945
- Bisschop, S. E., Jorgensen, J. K., van Dishoeck, E. F., & de Wachter, E. B. 2007, A&A, 465, 913
- Chen, X., Shen, Z-Q., Li, J-J., Xu Y., He, J-H., 2010, ApJ, 710, 150
- Chen, H-R., Liu, S-Y., Su, Y-N., Wang, M-Y., 2011, ApJ, accepted. (astro-ph:1110.0952)
- Charnley, S. B., Tielens, A. G. G. M., & Millar, T. J. 1992, ApJ, 399, L71
- Churchwell E., 2002, ARA&A 40, 27
- van Dishoek, E. & Blake, G. 1998, ARA&A, 36, 317
- Fuller, G. A., Williams, S. J., Sridharan, T. K. 2005, A&A, 442, 949
- Frerking, M. A., Langer, W. D & Wilson, R. W. 1982, ApJ, 262, 590
- Garden, P. R., Hayashi, M., Gatley, I. et al., 1991, ApJ, 374, 540
- Gong, H. & Ostrike, E. C., 2009, ApJ, 699, 230
- Jijina, J., & Adams, F. C. 1996, ApJ, 462, 874
- Hatchell, J., Millar, T. & Rodgers, S. 1998 A&A, 332, 695
- Keto, E., 2003, ApJ, 599, 1196

- Klaassen, P. D., & Wilson, C. D. 2007, *ApJ*, 663, 1092
- Krumholz, Mark R., Klein, Richard I., McKee, Christopher F., 2007, *ApJ*, 656,959
- Longmore, S. N., Pillai, T., Keto, E., Zhang, Q., Qiu, K., 2011, *ApJ*, 726, 97 (L11)
- Linsky, J. L. 1998, *Space Sci. Rev.*, 84, 285
- Mardones, D., et al., 1997, *ApJ*, 489, 719
- Mueller, K., Shirley, Y. L., Evans, N. J., II, Jacobson, H. R. 2002, *ApJS*, 143, 469
- Myers, P. C., Mardones, D., Tafalla, M., Williams, J. P., & Wilner, D. J. 1996, *ApJ*, 465, L133
- Ossenkopf, V., & Henning, T. 1994, *A&A*, 291, 943
- Omi, L., & Cesaroni, R. 1999, *A&A*, 352, 266
- Parise, B., Leurini, S., Schilke, P., Roueff, E., Thorwirth, S., Lis, D. C. 2009, *A&A*, 508, 737
- Pavlyuchenkov, Y., Wiebe, D., Schustov, B., Henning, T., Launhardt, R., & Semenov, D., 2008, *ApJ*, 689, 335
- Pillai, T., Wyrowski, F., Hatchell, J., Gibb, A. G., Thompson, M. A. 2007, *A&A*, 467, 207
- Purcell, C. R., Balasubramanyam, R., Burton, M. G., Walsh, A. J., Minier, V., Hunt-Cunningham, M. R., Kedziora-Chudczer, L. L., Longmore, S. N., Hill, T., Bains, I., and 25 coauthors, 2006, *MNRAS*, 367, 553
- Remijan, A., Sutton, E. C., Snyder, L. E., Friedel, D. N., Liu, S.-Y., & Pei, C.-C., 2004, *ApJ*, 606, 917
- Roberts, H., Fuller, G. A., Millar, T. J., Hatchell, J., Buckle, J. V. *A&A*, 381, 1026
- Rodgers, S. D., & Millar, T. J. 1996, *MNRAS*, 280, 1046
- Schnee, S., Kauffmann, J., Goodman, A., & Bertoldi, F. 2007, *ApJ*, 657, 838
- Schilke P., Walmsley C.M., Des Forêts G. P., Roueff E., Flower D. R., Guilloteau S., 1992, *A&A* 256, 595
- Shirley, Y. L., Evans, N. J., II; Young, K. E., Knez, C., Jaffe, D. T. 2003, *ApJs*, 149, 375
- Sollins, P. K., Ho, Paul T. P. 2005, *ApJ*, 630, 987
- Townes C. H., Schawlow A. L., 1955, *Microwave Spectroscopy*. McGraw, Hill, New York
- Tielens, A. G. G. M. 2005, *The Physics and Chemistry of the Interstellar Medium* (Cambridge University Press)
- Velusamy, T., Peng, R., Li, D., Goldsmith, P. F., Langer, William D. 2008, *ApJ*, 688, L87
- Walsh, A. J., Burton, M. G., Hyland, A. R., Robinson, G. 1998, *MNRAS*, 301, 640
- Wu, J., & Evans, N. J. II 2003, *ApJ*, 592, L79
- Wu, Y., Wei, Y., Zhao, M., Shi, Y., Yu, W., Qin, S., & Huang, M., 2004, *A&A*, 426, 503
- Wu, Y., Henkel, C., Xue, R., Guan, X., Miller, M. 2007, *ApJ*, 669, L37
- Wyrowski, F., Heyminck, S., Güsten, R., Menten, K. M. 2006, *A&A*, 454, L95
- Yorke, H. W., & Sonnhalter, C. 2002 *ApJ*, 569, 846
- Zhang, Q., Sridharan, T. K., Hunter, T. R., Chen, Y., Beuther, H., Wyrowski, F., 2007, *A&A*, 470, 269
- Zhou, S., Evans, N. J., II; Koempe, C., Walmsley, C. M. 2009, *ApJ*, 404, 232
- Zhou, S., Wu, Y., Evans, N. J., II, Fuller, Gary A., Myers, Philip C., 1989, *ApJ*, 346, 168

Table 1. General information of the single dish observations.

Instrument	PMO	CSO	JCMT
Obs. date	Dec 2009	May 2011	Aug 2005
Beam size	56''	30''	21''
η_{mb}	0.62	0.698	0.63
Pointing center	R.A.= 18:06:22.87 Dec.= -21:37:20.7	R.A.= 18:06:23.5 Dec.= -21:37:10.7	R.A.= 18:06:23.46 Dec.= -21:37:09.64

Table 2. observational parameters for the molecular lines from the single dishes.

Transition	Instrument	Atmosphere opacity	Band width (MHz)	ΔV_{res} (km s ⁻¹)	rms noise per channel (K)
¹² CO (2-1)	CSO	0.167	500	0.079	0.2
¹³ CO (2-1)	CSO	0.152	500	0.083	0.2
C ¹⁸ O (2-1)	CSO	0.149	500	0.083	0.2
¹² CO (1-0)	PMO	0.015	145	0.370	0.1
¹³ CO (1-0)	PMO	0.015	43	0.115	0.1
C ¹⁸ O (1-0)	PMO	0.015	43	0.115	0.2
HCN (3-2)	JCMT	0.111	160	0.088	0.5
H ¹³ CO ⁺ (3-2)	JCMT	0.067	160	0.090	0.3

Table 3. Observational parameters of the SMA.

Epoche	Frequency bands (GHz) LSB, USB	Bandpass Calibrator	Flux Calibrator	Phase & synthesized Calibrator	beam size (arcsec)	rms noise per channel (K) ^a
2007	(279.4,281.4), (289.4,291.4)	3c273	Neptune	1733-130,1911-201	7.0 × 5.8	0.110
2008	(219.5,221.5), (229.5,231.5)	3c454.3	Neptune	1733,1911	4.8 × 3.6	0.017
2009	(217.5,219.5), (227.5,229.5)	3c273	Uranus	1733,1911	6.8 × 3.6	0.150

a. For the unit conversion, 1 K=0.367, 1.43 and 1.04 Jy beam⁻¹ for the data in 2007, 2008, and 2009 respectively.

Table 4. Physical parameters of the dust core.

Parameter	Value	Unit
$F(3.6\mu\text{m})$	13 ± 0.1	mJy
$F(4.5\mu\text{m})$	78 ± 2	...
$F(5.8\mu\text{m})$	68 ± 2	...
$F(8.0\mu\text{m})$	10 ± 1	...
$F(24\mu\text{m})$	657 ± 40	...
$F(70\mu\text{m})$	196 ± 15	Jy
$F(450\mu\text{m})$	144 ± 15	...
$F(850\mu\text{m})$	15 ± 4	...
$F(1.3\text{mm})^a$	0.65 ± 0.03	...
$F(1.3\text{mm})^b$	2.9	...
	(450 μm / 1.3 mm) ^c	
$\langle r \rangle$	0.23 ± 0.05 / 0.08 ± 0.02	pc
M_{core}	1.5 ± 0.2 / 0.30 ± 0.01	$10^3 M_{\odot}$
$N(\text{H}_2)$	1.2 ± 0.2 / 0.95 ± 0.03	10^{24} cm^{-2}
$n(\text{H}_2)$	0.8 ± 0.1 / 3.8 ± 0.3	10^6 cm^{-3}

Note. To measure the integrated flux density of the dust core, we use the 4σ emission level as the integration area (aperture for the photometry). As an exception, we use the 4σ level of the $4.5\mu\text{m}$ emission as the area for all four IRAC bands, which roughly equals to the emission region with green color in Figure 4. The nearby point sources carefully excluded from this aperture.

a. The flux density of the SMA continuum observation.

b. The flux density extrapolated from the SED fitting (Figure 6).

c. For the last 4 parameters, the first and second values are derived from the $450\mu\text{m}$ and 1.3mm continuum data, respectively.

Table 5. Observed parameters of the molecular lines.

Molecule	Transition	Rest frequency (GHz)	E_u (K)	V_{LSR} (km s^{-1})	$T_{b,peak}$ (Kelvin)	ΔV_{FWHM} (km s^{-1})	$\int T_b dV$ (K km s^{-1})	τ^a	$\langle r \rangle^b$ (arcsec)	η_{bf}^c
(1)	(2)	(3)	(4)	(5)	(6)	(7)	(9)	(8)	(10)	(11)
$^{12}\text{CO}(\text{core})$	1–0	115.27120	5.5	37.0	26.0(1.5)	5.0(0.5)	134(15)	75	–	–
$^{12}\text{CO}(\text{outflow})$	1–0	37.3	4.0(1.5)	9.2(1.0)	37(5)	0.15	–	–
$^{12}\text{CO}(\text{core})$	2–1	230.53800	17	37.0	32.0(0.5)	5.5(0.5)	240(30)	68	–	–
$^{12}\text{CO}(\text{outflow})$	2–1	37.0	5.0(0.5)	9.0(0.5)	45(6)	0.15	–	–
HCN(core)	3–2	265.88643	26	38.5	12.0(0.2)	6.2(0.5)	73(9)	0.78/0.10	12	1
HCN(outflow)	3–2	39.5	0.8(0.2)	15.0(1.0)	12(5)	0.053/0.007	–	–
^{13}CO	1–0	110.20135	5.3	35.0	12.4(0.5)	6.8(0.1)	85(10)	0.85	–	–
^{13}CO	2–1	220.39968	16	35.0	8.5(0.5)	7.5(0.5)	60(15)	0.70	–	–
C^{18}O	1–0	109.78217	5.3	37.0	4.5(0.5)	5.6(0.4)	23(4)	0.17	–	–
$\text{C}^{18}\text{O}(\text{CSO})$	2–1	219.56036	16	38.0	6.0(0.3)	5.5(0.4)	34(3)	0.140	–	–
$\text{C}^{18}\text{O}(\text{SMA})$	2–1	219.56036	16	38.0	5.2(0.02)	4.8(0.3)	30(3)	0.423/0.065	3.4	1
CH_3OH	$8_0 - 7_1$	220.07849	97	37.5	1.6(0.22)	5.0(1.3)	8(2)	0.209/0.028	3.1	1
CH_3OH	$8_{-1} - 7_0$	229.75880	89	37.0	3.42(0.15)	6.0(0.3)	18.0(1.5)	0.453/0.059	2.8	1
CH_3OH	$3_{-2} - 4_{-1}$	230.02706	39	38.5	0.9(0.03)	6.0(0.4)	5.8(0.5)	0.036/0.004	3.2	1
CH_3OH	$10_2 - 9_3$	231.28110	165	39.0	0.53(0.06)	6.0(0.9)	3.4(0.5)	0.087/0.011	2.2	0.95
CH_3OH	$9_{-1} - 8_0$	278.30451	110	38.0	1.39(0.06)	5.4(0.4)	7.2(0.8)	0.245/0.031	2.9	0.89
CH_3OH	$2_{-2} - 3_{-1}$	278.34226	33	39.0	0.24(0.02)	5.5(0.4)	1.5(0.2)	0.045/0.006	3.2	1
CH_3OH	$21_{-2} - 20_{-3}$	278.48023	563	40.0	0.09(0.02)	4.0(0.5)	0.4(0.05)	0.024/0.002	2.2	0.48
CH_3OH	$15_{7,8} - 16_{6,11}$	288.07677	523	37.5	0.24(0.02)	5.5(0.3)	1.2(0.2)	0.102/0.012	2.3	0.52
CH_3OH	$14_4 - 15_3$	278.59906	340	39.5	0.29(0.02)	6.3(1.3)	1.8(0.2)	0.073/0.009	2.5	0.62
CH_3OH	$11_2 - 10_3$	279.35191	191	39.5	0.28(0.02)	6.5(1.9)	2.3(0.3)	0.081/0.009	2.8	0.78
CH_3OH	$4_3 - 5_2$	288.70557	71	39.5	0.28(0.02)	6.5(1.5)	1.8(0.3)	0.068/0.008	2.8	0.77
DCN	3–2	217.23854	81	39.0	2.1(0.4)	3.5(0.2)	7.5(1)	0.132/0.018	3.1	0.92
DCN	4–3	289.64492	35	39.0	1.0(0.04)	3.5(0.2)	5.0(0.4)	0.072/0.009	3.3	1
C^{34}S	6–5	289.20907	38	39.0	1.4(0.02)	4.5(0.5)	6.5(0.7)	0.123/0.016	3.3	1
H^{13}CO^+	3–2	260.25534	25	38.0	4.7(0.3)	4.4(0.3)	20(2)	0.260/0.033	–	–

Note. The ^{12}CO , ^{13}CO lines, and C^{18}O lines are from the PMO and CSO observations (see Table 2). The C^{18}O (2–1) line from the SMA observation is also presented. The HCN and H^{13}CO^+ lines are observed with the JCMT. For the double-peaked lines, including HCN (3–2), ^{12}CO (2–1) and (1–0), and two CH_3OH lines ($E_u = 191$ K and $E_u = 523$ K), the parameters are measured from the fitted spectra, while for the single-peak lines, we directly measured the observed spectra.

a. The optical depth at the line peak. For the transitions with two values, the first and second one are the results for $T_{\text{rot}} = 20$ K and 114 K, respectively (see Section 4.4). While for the CO (1–0) and (2–1), the optical depths are calculated from comparing their isotopic lines (Section 4.3).

b. The effective radius of the emission region, measured from the deconvolved average radius of the 10% contour region (1/2 times the value). An exception is the HCN (3–2), for which we directly measured the 50 % contour. The average uncertainty level is ~ 2 arcsec. For G8.68 at $D = 4.5$ kpc, 1 arcsec = 0.02 pc.

c. The beam filling factor, calculated from the ratio between the area of the deconvolved emission region ($\pi \langle r \rangle^2$) and the beam size.

Table 6. Collum density and abundance of the molecular species.

Molecule (X)	$T_{\text{rot}} = 20 \text{ K}^a$		$T_{\text{rot}} = 130 \text{ K}$	
	$N_{\text{T}}(\text{X})$ (cm^{-2})	$f(\text{X})$	$N_{\text{T}}(\text{X})$ (cm^{-2})	$f(\text{X})$
C^{18}O	$(2.2 \pm 0.3) \times 10^{16}$	$(2.3 \pm 0.3) \times 10^{-8}$	$(5.4 \pm 0.6) \times 10^{16}$	$(5.6 \pm 0.7) \times 10^{-8}$
CH_3OH^b	$(1.8 \pm 0.2) \times 10^{15}$	$(2.0 \pm 0.2) \times 10^{-9}$	$(5.3 \pm 0.6) \times 10^{15}$	$(5.8 \pm 0.6) \times 10^{-9}$
C^{34}S	$(2.3 \pm 0.3) \times 10^{13}$	$(2.5 \pm 0.4) \times 10^{-11}$	$(2.6 \pm 0.3) \times 10^{13}$	$(2.9 \pm 0.4) \times 10^{-11}$
H^{13}CO^+	$(9.5 \pm 1.0) \times 10^{12}$	$(7.9 \pm 0.7) \times 10^{-12}$	$(1.7 \pm 0.2) \times 10^{13}$	$(1.4 \pm 0.1) \times 10^{-11}$
HCN	$(5.6 \pm 0.5) \times 10^{14}$	$(4.6 \pm 0.3) \times 10^{-10}$	$(1.1 \pm 0.1) \times 10^{15}$	$(8.9 \pm 0.8) \times 10^{-10}$
DCN	$(3.1 \pm 0.1) \times 10^{13}$	$(3.4 \pm 0.2) \times 10^{-11}$	$(5.6 \pm 0.3) \times 10^{13}$	$(6.2 \pm 0.5) \times 10^{-11}$
[DCN/HCN] ^c	–	0.07 ± 0.01	–	0.07 ± 0.01

a. A lower limit as suggested by the dust continuum SED.

b. At $T_{\text{rot}} = 20$ K, $N_{\text{T}}(\text{CH}_3\text{OH})$ is derived from $3_{-2} - 4_{-1}$ line.

c. Abundance ratio between DCN and HCN.

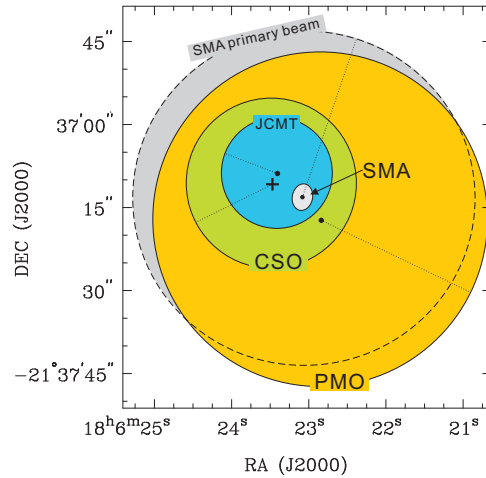


Figure 1. The beam size and pointing center of each instrument. The cross symbol marks the center of the 1.3 mm dust core (Figure 4) which is coincident with the CSO pointing center. The white ellipse is the synthesized beam of the SMA in the 2008 observation, and the gray filled circle is the primary beam. The JCMT beam size is for the frequency of 289 GHz.

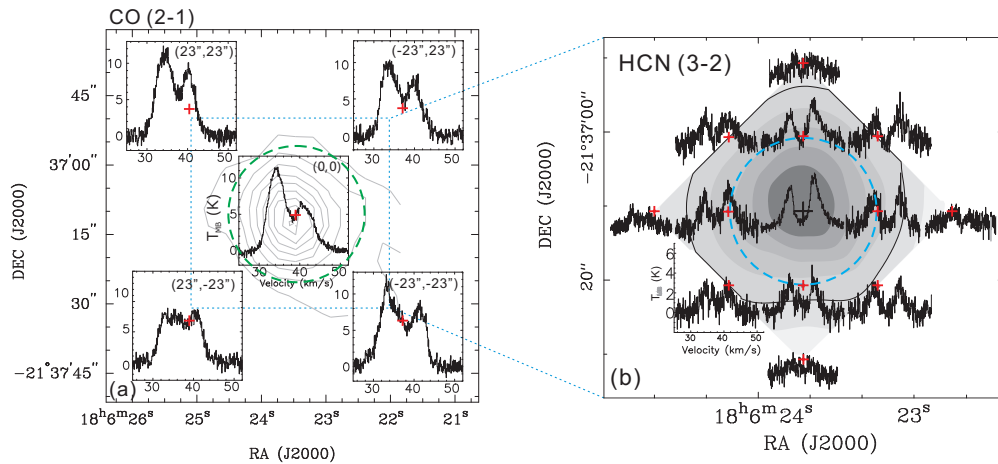


Figure 2. (a) Grid spectra of ^{12}CO (2–1) observed from the CSO. The red cross labels the pointing center of each spectrum. The gray contours are the SCUBA 450 μm emission (specified in Figure 4). The green dashed line represents the beam size. (b) Grid spectra of HCN (3–2) observed from the JCMT. The red cross labels the pointing center of the each spectrum. The intensity map (gray scales) is made from interpolating the line intensity at each point. The integration for the spectra is from 25 to 50 km s^{-1} . The gray-scale levels are from 30 % to 90 % of the maximum intensity (46.8 K km s^{-1}). The thick contour is the 50 % level. The blue dashed circle is the beam size.

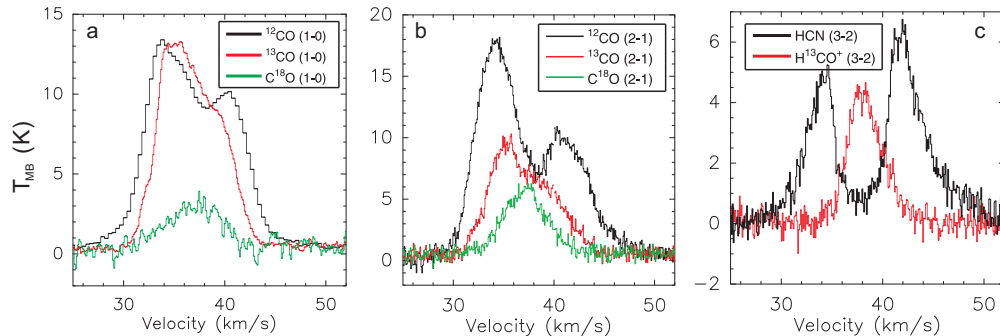


Figure 3. Molecular lines observed from the PMO, CSO, and JCMT, which are shown in left, middle, and right panels, respectively. The observing centers and the beam size of each telescope are shown in Figure 1.

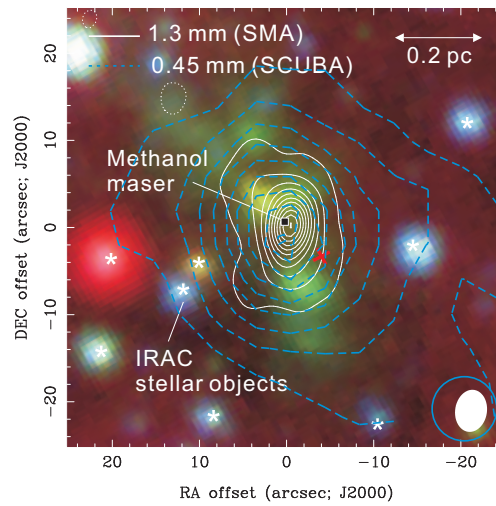


Figure 4. Continuum emissions detected towards G8.68 from infrared to millimeter wavelengths. The image is centered at the emission peak of the 1.3 mm continuum, the coordinates of which are RA.(J2000)= $18^{\text{h}}06^{\text{m}}23.5^{\text{s}}$ and Decl.(J2000)= $-21^{\circ}37'10.7''$. The white contours are the 1.3 mm emission observed from the SMA. The contour levels are -4, 4, 14, 24... 104 σ ($0.003 \text{ Jy beam}^{-1}$). The -4 σ contour is due to the insufficient (u,v) coverage and is plotted in dotted line. The square denotes the strongest CH_3OH maser (Walsh et al. 1998). The dashed contours are the JCMT/SCUBA 450 μm emission. The levels are 4, 8, 12... 36 σ (1.2 Jy beam^{-1}). The IRAC 3.6 (blue), 4.5 (green) and 8.0 (μm) images are shown together in RGB colors (also seen in Figure 1 and 2 in L11). The red cross labels the SMA phase center. The synthesized beam of the SMA (white ellipse) and SCUBA (blue circle) beam are plotted in the right corner.

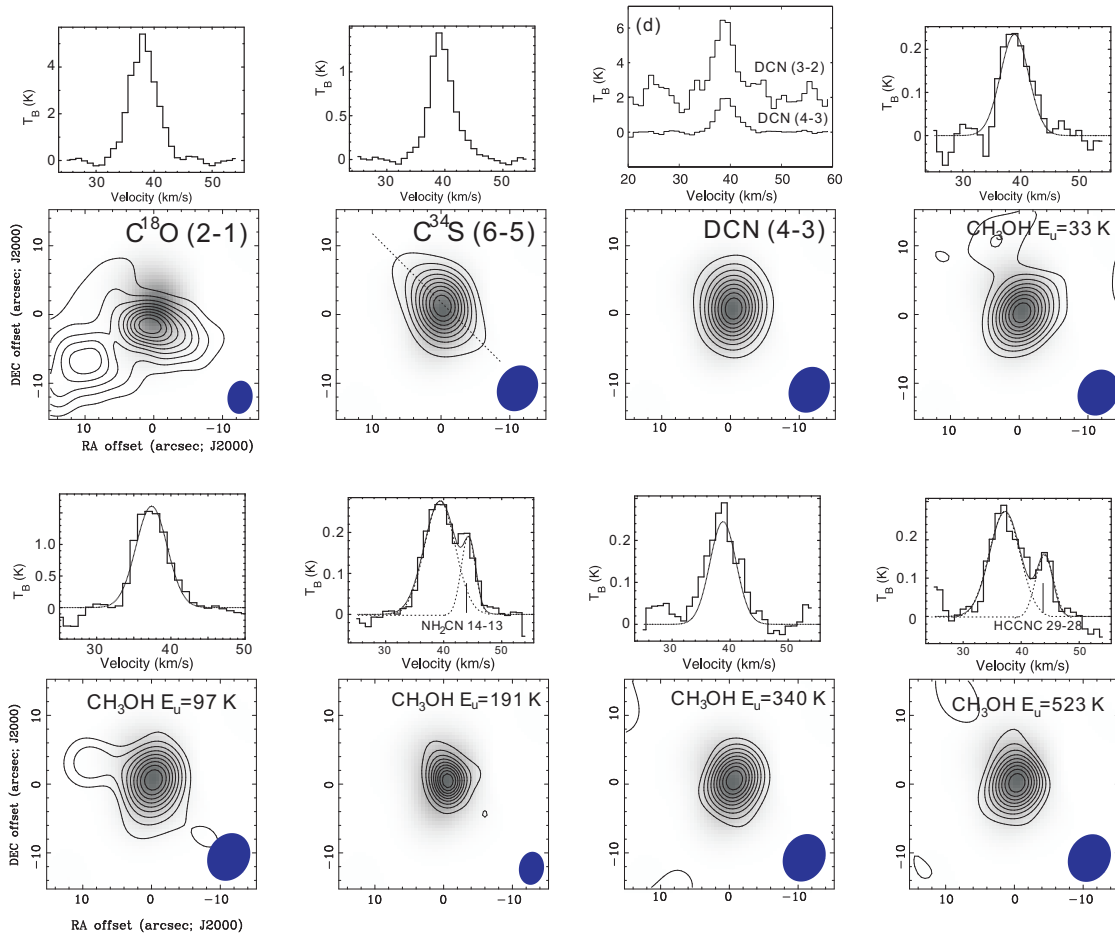


Figure 5. Molecular lines and integrated images observed from the SMA. For each transition, the contours are 10, 20... 90 percent of the peak intensity. The integration range is $(37, 43) \text{ km s}^{-1}$ for all the transitions except the two blended CH_3OH lines. For these two lines the integration range is $(37, 40) \text{ km s}^{-1}$ as to eliminate the contamination. The dashed line in the C^{34}S labels the orientation of the outflow in L11. The DCN (3–2) line is shifted above the zero level for 2 K. The negative contours due to the missing flux are omitted to more clearly show the emission features. The gray-scale image in each panel is the SMA 1.3 mm continuum.

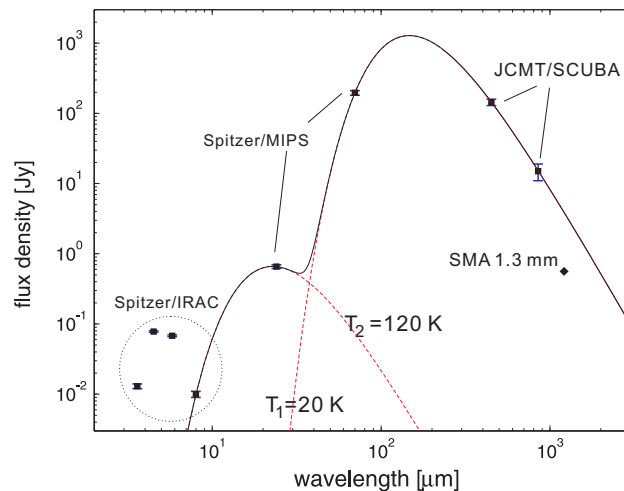


Figure 6. The spectra energy distribution of the dust core. The black squares with error bars are the data points (the SMA 1.3 mm flux density is marked with the diamond). The black line is the fitted SED curve. The red dashed lines are the SEDs of the two temperature components, with $T_d = 20 \text{ K}$ and 120 K , respectively.

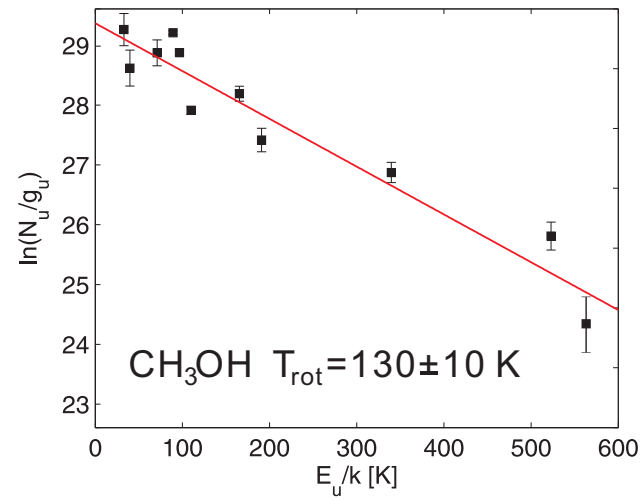


Figure 7. The rotation diagram of the CH_3OH lines. The black squares with error bars are the data points. The red line is the least-square fit.

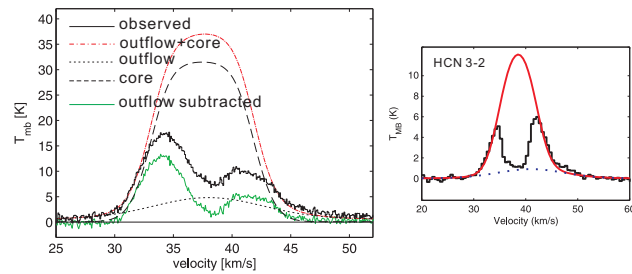


Figure 8. The two-component fit to the ^{12}CO (2–1) spectrum towards the center. The meaning of each line type is labeled in the legend.